Impurity position and lattice distortion in a Mn-doped Bi_2Te_3 topological insulator investigated by x-ray fluorescence holography and x-ray absorption fine structure

Shinya Hosokawa,[1,*] Jens Rüdiger Stellhorn,[1] Tomohiro Matsushita,[2] Naohisa Happo,[3] Koji Kimura,[4] Koichi Hayashi,[4] Yoshihiro Ebisu,[5] Toru Ozaki,[5] Hiroyuki Ikemoto,[6] Hiroyuki Setoyama,[7] Toshihiro Okajima,[7] Yoshitaka Yoda,[2] Hirofumi Ishii,[8] Yen-Fa Liao,[8] Mamoru Kitaura,[9] and Minoru Sasaki[9]

[1]*Department of Physics, Kumamoto University, Kumamoto 860-8555, Japan*
[2]*Japan Synchrotron Radiation Research Institute (JASRI), Sayo, Hyogo 679-5198, Japan*
[3]*Graduate School of Information Sciences, Hiroshima City University, Hiroshima 731-3194, Japan*
[4]*Department of Physical Science and Engineering, Nagoya Institute of Technology, Nagoya 466-8555, Japan*
[5]*Research Center for Condensed Matter Physics, Graduate School of Science and Technology, Hiroshima Institute of Technology, Hiroshima 731-5193, Japan*
[6]*Department of Physics, Faculty of Science, University of Toyama, Toyama 930-8555, Japan*
[7]*Kyushu Synchrotron Light Research Center, Tosu 841-0005, Japan*
[8]*National Synchrotron Radiation Research Center, Hsinchu 30076, Taiwan*
[9]*Department of Physics, Faculty of Science, Yamagata University, Yamagata 990-8560, Japan*

(Received 28 August 2017; published 26 December 2017)

Mn $K\alpha$ x-ray fluorescence holography (XFH) measurements were performed on a single crystal of a $Bi_2Te_3Mn_{0.1}$ topological insulator at 100 and 300 K to search for the impurity sites of the Mn atoms in this functional crystal. The three-dimensional atomic images were reconstructed using an L_1-regularized linear regression. X-ray absorption fine-structure (XAFS) experiments were also carried out at 30–300 K to obtain additional structural information. The local structural information was obtained from these data, such as the positions of the Mn impurity sites, the Mn-Te interatomic distances, the lattice distortions, and the positional fluctuations around the impurity Mn atoms. The possible Mn impurity sites are twofold, i.e., an interlayer site with an octahedral symmetry and a substitutional site of Te on the layer surface. A distinct temperature dependence is seen in the positional fluctuations of the impurity Mn atoms in the substitutional site. These findings for the impurity sites cannot be easily obtained by diffraction or XAFS experiment in the usual way, but only using a combination of the XFH and XAFS measurements.

DOI: 10.1103/PhysRevB.96.214207

I. INTRODUCTION

In the past, Bi_2Te_3 was well known as a thermoelectric material having a large value of thermopower [1,2]. Nowadays, this material has also achieved much attention as a topological insulator (TI), where the so-called Dirac electrons with an almost zero mass can conduct on the surface of this material [3]. For this reason, Bi_2Te_3 is promising as a raw material for very fast and energy-saving computer systems in the future.

TIs have insulating energy gaps in bulk but gapless surface states on the sample boundary that are protected by time-reversal symmetry. The surface of three-dimensional (3D) TI consists of an odd number of Dirac cones. The existence of the surface states with a Dirac cone was expected in Bi_2Te_3 based on an *ab initio* molecular-dynamics (MD) simulation by Zhang *et al.* [4]. The electronic structure of Bi_2Te_3 was measured using angle-resolved photoemission spectroscopy (ARPES) [5]. Due to the insufficient angle resolution of the obtained spectra, however, the Dirac cone was not detected experimentally even by changing the concentrations of Bi and Te. A recent ARPES work with better angle and energy resolutions by Chen *et al.* [6] revealed that the surface state of Bi_2Te_3 consists of a single nondegenerate Dirac cone.

Bi_2Te_3 is essentially a *p*-type degenerate semiconductor. By adding electrons, for example, with increasing Te concentration, it has a bulk-insulating character with a TI nature, and then it changes to an *n*-type degenerate semiconductor [3]. The surface states were observed in *p*-type doped Bi_2Te_3 using high-resolution ARPES [7]. However, the TI properties in the $Bi_2Te_{3+\delta}$ alloy easily decay within a time scale of a few months due to surface contaminations, which was confirmed by time-dependent ARPES spectra [7]. Thus, this material is not suitable for stable applicational uses.

Recently, Kim *et al.* [8] found that $Bi_2Te_3Fe_x$ alloys have a similar TI behavior. The TI phase appears between $x = 0.03$ and 0.10. They found two interesting features as a TI. First, the lifetime of the TI properties is extremely long, which is very important for the applications. Second, the Dirac electrons are not scattered by impurities (clean surface Dirac electrons), which was realized by a magnetoresistance measurement at low temperatures.

Mn-doped Bi_2Te_3 alloys show excellent TI properties similar to the Fe-doped ones. The existence of the Dirac cone was confirmed in Mn-doped Bi_2Te_3 by an ARPES investigation [9]. Moreover, these alloys are suitable for investigating the atomic structures of the series of the transition-metal (TM)-doped Bi_2Te_3 TI alloys since a good quality of the single crystal can be easily obtained.

The undoped Bi_2Te_3 has a layer structure with a rhombohedral form (space group: $R\bar{3}m$) with $a = 0.4395$, $c =$

*hosokawa@sci.kumamoto-u.ac.jp

 ©2017 American Physical Society

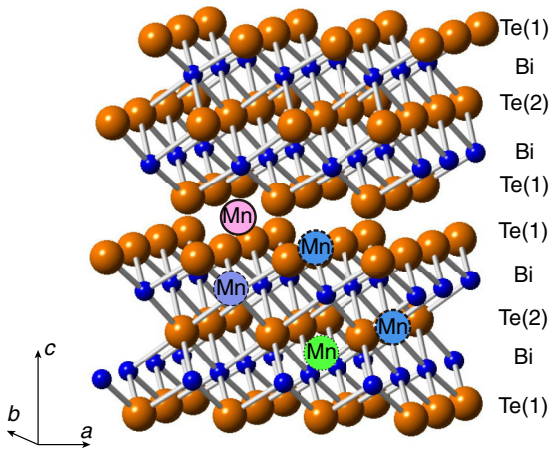

FIG. 1. Two layers in the undoped Bi_2Te_3 hexagonal crystal [10]. Large and small balls indicate Te and Bi atoms, respectively. The circles are possible impurity Mn sites of interlayer octahedral pocket (pink solid circle), interstitial (green dotted circle), substitutional with Bi (light blue thin dashed circle), and Te (dark blue thick dashed circles).

1.04591 nm, and $\alpha = 77.872^\circ$, or in the standardized form, with a hexagonal form with $a = 0.4395$ and $c = 3.044$ nm, where three layers are located in the unit cell [10]. Figure 1 shows two layers of the Bi_2Te_3 crystal. There are two sites for the Te atoms in the layer. One is on the surface of the layers, Te(1), where a van der Waals force combines the layers, and another is at the center of the layers, Te(2), which connects with Bi atoms by a covalent-ionic mixed binding.

From a structural point of view, two important questions arise on the impurity doping into the Bi_2Te_3 crystal. The first is where the impurity Mn atoms are located in the crystal. Most researchers believe that the interlayer (solid circle in Fig. 1) would be the most plausible site for the Mn impurities. However, there is no experimental proof to exclude the interstitial site (dotted circle) or the substitutional site with Bi (thin dashed circle) or Te (thick dashed circles) atoms. The second question is how the impurities induce lattice distortions in the crystal. These questions cannot be easily solved using diffraction experiments because the impurity atoms have no long-range periodic order in the crystal.

To search for the impurity positions, an x-ray absorption fine-structure (XAFS) study was carried out at room temperature on epitaxial layers of $(Bi_{1-x}Mn_x)_2Te_3$ substitutional crystals ($0.04 \leqslant x \leqslant 0.13$) manufactured using molecular-beam epitaxy (MBE) by Růžička *et al.* [9]. From the detailed analysis of the XAFS results combined with x-ray diffraction (XRD), they concluded that the Mn atoms occupy interlayer positions within the van der Waals gaps of the interlayer sites and are surrounded octahedrally by Te atoms of the adjacent layers. They excluded the substitutional positions of the Bi sites within the layers. In this configuration, the Mn-Te and Mn-Bi interatomic distances are 0.292 ± 0.004 and 0.304 ± 0.010 nm, respectively. As pointed out by the authors, however, the fits in the low distance (r) region were insufficient, and another impurity site was not excluded from their results.

A similar attempt was made by Ghasemi *et al.* [11], who carried out an XAFS study on an epitaxial layer of $(Bi_{0.975}Mn_{0.025})_2Te_3$ substitutional crystals in combination with electron-energy-loss spectroscopy (EELS), scanning transmission electron microscopy (STEM), and first-principles density-functional studies. They concluded a different result that Mn is a "substitutional dopant of Bi and Te" and also resides in the van der Waals gap.

The Mn impurity positions in the Bi_2Te_3 crystal were also discussed very recently by Carva *et al.* [12] using an *ab initio* MD simulation to obtain electronic density of states features, magnetic moments, and transport properties. It was concluded that the doped Mn atoms are located at the substitutional positions with Bi and the interstitial van der Waals gap positions. However, the substitutional positions with Te would be intuitively excluded as the candidate of their calculations.

More recently, core-level x-ray photoelectron, x-ray absorption, and x-ray emission spectroscopies were measured by Leedahl *et al.* [13] together with the theoretical calculations of these spectra using a density-functional theory for investigating the preferred oxidation state of $3d$-metal impurities in the Bi_2Te_3 crystal. They found that about 90% of the Mn impurities have the 2+ oxidation state, and there are mostly no metallic signals. From the experimental results together with the good agreement with the theoretical spectra, they concluded that the Mn impurities in Bi_2Te_3 substitute into the Bi site in a 2+ oxidation site. However, it is not clear for us why they could exclude the possibility of the interstitial sites in the van der Waals gap or the substitutional sites with the Te atoms due only to the determination of the 2+ oxidation state of the Mn impurities.

Detailed investigations on the impurity sites of TMs were also carried out in Bi_2Se_3 crystal by XAFS and other techniques, such as additional doping with Cr, Co, Ni, Cu [14], and Fe [15], and Bi-substitutional doping with Cr [16], Fe, Mn, and Cr [17]. It was commonly concluded that the impurity TM atoms substitute for the Bi atoms, although the divalent TM^{2+} atoms enter the trivalent Bi^{3+} sites. In general, compared with the host $BiSe_4$ atomic arrangements, large lattice distortions are induced around the impurity TM atoms. The other possibilities are also intensively discussed, such as the interlayer sites with some octahedral and tetrahedral atomic configurations with large lattice distortions.

Since the structural information from extended XAFS (EXAFS) measurements is limited to be mainly from the one-dimensional radial direction, the measurements can involve the 3D atomic configurations around the impurity atoms only in combination with other experimental methods, such as XRD [9,11,14,16], x-ray absorption near-edge structure (XANES) [9,11,15–17], EELS [11], high-angle annular dark-field scanning transmission electron microscopy (HAADF-STEM) [11], and *ab initio* calculation [15]. It was, however, difficult to reach a final conclusion for determining the impurity sites, and an excellent method to clarify the 3D atomic configurations is still required.

X-ray fluorescence holography (XFH) is a newly developed technique for atom-resolved structure characterizations of materials, and it enables one to draw 3D atomic images around a specific element emitting fluorescent x rays [18]. Due to the interference between the direct incident x rays and those scattered by the surrounding atoms, the fluorescent x-ray intensity from the emitter slightly modulates with the

incident x-ray angles by some 0.1%, from which 3D images of the neighboring atoms can be obtained by simple Fourier-transform-like approaches without any special atomic models. To solve the presently existing questions, XFH is very useful.

We have recently carried out a Mn $K\alpha$ XFH measurement on the $Bi_2Te_3Mn_{0.1}$ crystal at 300 K, and the preliminary results were already published elsewhere [19]. The reconstructed atomic images around the central Mn atom show only a hexagonal configuration of the second-neighboring atoms on the (001) plane. Their atomic positions are, however, slightly longer from the central atom with respect to those in the undoped Bi_2Te_3 crystal. From this observation, it was concluded that a large number of the Mn impurities are located at the *substitutional* sites of the Bi or Te atoms. Note that it was difficult to determine from only this XFH result whether the Mn atoms are substituted for Bi or Te since the local environments around the Bi and Te atoms are identical on the (001) plane of the undoped Bi_2Te_3 crystal.

Moreover, two questions still remain unsolved in the experimental results: (i) Why could the nearest-neighboring atoms not be observed on the (001) plane with different z values, even though these atoms should be inside the rigid layer if the speculation of the substitutional impurity site was correct. (ii) Why are the second-neighboring atoms shifted toward the longer positions from the lattice positions of the undoped Bi_2Te_3 crystal, even though the typical Mn-Te interatomic distance is much shorter than the Bi-Te bond lengths of 0.3062–0.3255 nm in the undoped Bi_2Te_3 hexagonal crystal [10], i.e., 0.2916 nm with the NiAs structure under ambient conditions [20], 0.2744 nm with the zinc-blende structure only for thin films [21], or 0.2379–0.2491 nm with the FeAs structure under pressure [22] in the MnTe crystal.

To answer these questions, an XFH experiment has been performed on the same $Bi_2Te_3Mn_{0.1}$ crystal at 100 K since the low temperature may suppress thermal agitations of the atomic positions. The holographic data were analyzed using an algorithm of an L_1 regularized linear regression representing a sparse modeling approach. From these efforts, some additional atomic images could be clearly visualized, which enabled us to obtain further information on the impurity sites of the Mn atoms in the Bi_2Te_3 crystal. In addition, XAFS measurements were performed on the same sample at 30–300 K. In this paper, we will present an insight into the bimodal impurity positions and the corresponding lattice distortions induced by the Mn doping in the layered Bi_2Te_3 hexagonal crystal.

II. EXPERIMENTAL PROCEDURE

A single crystal $Bi_2Te_3Mn_{0.1}$ was grown by a modified Bridgman method, where appropriate amounts of Bi_2Te_3 and Mn powders were melted and crystallized in an evacuated quartz ampoule several times by slow cooling. The sample was cooled from 850 to 550 °C with a cooling rate of −10 °C/h. The crystal was cleaved and polished so as to have a flat (001) surface with an area larger than 3×3 mm^2. The crystallinity of the sample was examined by taking a Laue photograph, and the concentration and homogeneity over the sample were confirmed within the experimental errors by an electron-probe microanalysis.

The Mn $K\alpha$ XFH measurements were carried out on the $Bi_2Te_3Mn_{0.1}$ single crystal at 100 and 300 K using a cryostream apparatus at the beamline BL6C of the Photon Factory in the High Energy Accelerator Research Organization (PF-KEK), Tsukuba, Japan. The sample was placed on a two-axes table of a diffractometer. The measurement was performed in inverse mode by changing two axes, the incident angle of $0^\circ \leqslant \theta \leqslant 75^\circ$ in steps of 1.00° and the azimuthal angle of $0^\circ \leqslant \phi \leqslant 360^\circ$ in steps of about 0.35°. Incident x rays were focused on the (001) surface of the sample. Mn $K\alpha$ fluorescent x rays were collected using an avalanche photodiode detector via a cylindrical graphite crystal energy-analyzer. The XFH signals were recorded at eight different incident x-ray energies from 7.0 to 10.5 keV in steps of 0.5 keV. Details of the experimental setup are given elsewhere [18].

The holographic oscillation data were obtained by subtracting the background from the fluorescent x-ray intensities and normalizing them with the incident x-ray intensities measured with an ion chamber. To avoid any foresight on the impurity positions, usual extensions of the holographic data to the 4π sphere using the crystal symmetry and the measured x-ray standing wave (XSW) lines were not carried out, and only the threefold rotational symmetry was taken into account. Then, the backside of the hologram was added by copying the measured hologram and turning by 180° by referring to the symmetry of the undoped Bi_2Te_3 crystal. Note that since the obtained hologram does not cover perfectly the 4π solid angle, i.e., the data in $75^\circ < \theta < 105^\circ$ are missing, atomic images on the (001) plane including the central Mn atom ($z = 0$) can be distorted in the angular direction if the usual Barton's algorithm [23] is used for the reconstruction of the atomic image as explained in Ref. [24] in detail.

From the obtained holograms, 3D atomic configuration images were usually reconstructed using Barton's algorithm [23] by superimposing the images Fourier-transformed from different incident x-ray energies, which can highly suppress the appearance of twin images and improve the statistical qualities [18,25]. In the present study, however, a number of unphysical artifacts appear in the reconstructed images by Barton's algorithm, due probably to the missing area of the holographic data in $75^\circ < \theta < 105^\circ$, and the complex atomic configurations are observed around the Mn impurity atoms. Thus, we employed a more sophisticated analysis of a "scattering pattern matrix extraction algorithm using an L_1 regularized linear regression" (SPEA-L1) by Matsushita [26], which represents a sparse modeling approach to the experimental holographic data. The details are given in the next section.

The XAFS experiments were carried out near the Mn K absorption edge (6.540 keV) at the beamline BL11 of the Kyushu Synchrotron Light Research Center, Tosu, Japan. The XAFS data were collected in the temperature range 30–300 K in fluorescence mode. X rays emitting from a binding magnet source were monochromatized using a double Si(111) crystal. The incident x-ray intensity was measured using an ion chamber, and fluorescent x-ray intensity was detected using a 19-channel pure Ge solid-state detector.

The resultant data were analyzed using the ARTEMIS software package [27] in combination with the FEFF program [28]. A Fourier transform analysis was carried out for the

XAFS functions $\chi(k)$, which were extracted from the raw absorption data μ as a function of the wave number of the photoelectrons, k.

Then, the neighboring area of the Fourier transforms of $k^2\chi(k)$, $|F(r)|$, was inverse-Fourier-transformed to obtain $k^2\chi(k)$ concerning only the corresponding neighboring atoms. In each Fourier transform procedure, Hanning window functions were always used to reduce the truncation errors in the results. Using a theoretical formula expressed as

$$\chi(k) = S_0^2 \sum_i \frac{N_i}{kr_i} f_i(k,\pi) \sin[2kr_i + \phi_i(k)] e^{-2[\sigma_i^2 k^2 + r_i/\lambda(k)]}, \tag{1}$$

fits were performed to obtain the structural parameters. Here, S_0^2 is the amplitude reduction factor; N_i, r_i, $f_i(k,\pi)$, σ_i, and $\phi_i(k)$ are, respectively, the coordination number, the interatomic distance, the backscattering atomic form factor, the Debye-Waller factor, and the phase shift of the neighboring atom i; and λ is the mean free path of photoelectrons. The $f_i(k,\pi)$, $\phi_i(k)$, and $\lambda(k)$ functions were calculated using the FEFF program package [28] by assuming a model atomic configuration around the central atom. We made the corrections of the self-absorption effect intrinsic to the fluorescent XAFS measurements using the Athena program in the IFEFFIT software package [27]. After that, the S_0^2 values were set to be the same values of about unity at all of the temperatures measured.

III. SPEA-L_1 ANALYSIS

Recently, local atomic structures have been studied intensively by inverse XFH using synchrotron radiation facilities. The 3D atomic image is reconstructed from a hologram using a calculation, and the performance of the algorithm used for the reconstruction is very important. Barton's method [23] based on the Fourier transform is typically used for this. However, images reconstructed by this method sometimes contain considerable artifacts, such as in the present case.

The recording process used in inverse XFH is as follows. When a sample is irradiated with x rays with an energy higher than an absorption edge of a constituent element, it emits fluorescent x rays. Part of the incident x rays is scattered by surrounding atoms, and the scattered spherical waves (object wave) interfere with the incident plane wave (reference wave). The hologram is measured as the intensity modulation of the fluorescent x rays with incident angles, and it is given by

$$\eta(\boldsymbol{k}) \propto -\int \rho(\boldsymbol{r}) \frac{\cos(kr - \boldsymbol{k}\cdot\boldsymbol{r})}{r} d\boldsymbol{r}, \tag{2}$$

where $\eta(\boldsymbol{k})$ and $\rho(\boldsymbol{r})$ are the hologram and electron density functions, respectively, and the origin of $\boldsymbol{r}$ is the fluorescence emitter atom.

Barton's method is given by

$$u(\boldsymbol{k}) = -r \int \eta(\boldsymbol{k}) \cos(kr - \boldsymbol{k}\cdot\boldsymbol{r}) d\boldsymbol{k}, \tag{3}$$

where $u(\boldsymbol{r})$ is the reconstructed image. To perfectly reconstruct the 3D atomic image, an infinite number of holograms are, in principle, necessary by changing k of the incident x rays from 0 to ∞. However, the integral by k is replaced by the sum of a limited number of holograms with different k values, and this is the main reason for the appearance of artifacts in the reconstructed atomic image. To solve this problem, Matsushita developed an algorithm, SPEA-L1 [26], which is based on the inverse problem and sparse modeling.

When the atomic form factor f is introduced, Eq. (2) is expressed as

$$\eta(\boldsymbol{k}) = -\sum_i \frac{f(\theta_{\boldsymbol{a}_i,\boldsymbol{k}}) \cos(ka_i - \boldsymbol{k}\cdot\boldsymbol{a}_i)}{a_i}, \tag{4}$$

where $\boldsymbol{a}_i$ represents the position of the ith atom, and $\theta_{\boldsymbol{a}_i,\boldsymbol{k}}$ is the angle between $\boldsymbol{a}_i$ and $\boldsymbol{k}$. This equation can be extended by introducing the atomic distribution function $g(\boldsymbol{r})$ as

$$\eta(\boldsymbol{k}) = -\int g(\boldsymbol{r}) f(\theta_{\boldsymbol{r},\boldsymbol{k}}) \cos(kr - \boldsymbol{k}\cdot\boldsymbol{r}) d\boldsymbol{r}. \tag{5}$$

The $g(\boldsymbol{r})$ function is sparse, and L_1-regularized linear regression [29] is applicable. By using voxels for describing $g(\boldsymbol{r})$ [30], Eq. (5) is modified as

$$\eta(\boldsymbol{k}_j) = -\sum_i g(\boldsymbol{r}_i) f(\theta_{\boldsymbol{r}_i,\boldsymbol{k}_j}) \cos(k_j r_i - \boldsymbol{k}_j\cdot\boldsymbol{r}_i). \tag{6}$$

To obtain $g(\boldsymbol{r}_i)$ by the L_1-regularized linear regression, its evaluation function is given by

$$E = \sum_j |\eta(\boldsymbol{k}_j) - \hat{\eta}(\boldsymbol{k}_j)|^2 + \lambda \sum_i |g(\boldsymbol{r}_i)|, \tag{7}$$

where $\hat{\eta}(\boldsymbol{k}_j)$ is the experimental hologram and λ is a penalty parameter.

To obtain the atomic image $g(\boldsymbol{r}_i)$, the minimization of E is performed by the iterative calculation of

$$g^{(n+1)}(\boldsymbol{r}_i) = g^{(n)}(\boldsymbol{r}_i) - \alpha \frac{\partial E^{(n)}}{\partial \boldsymbol{r}_i}, \tag{8}$$

where n is the index for iteration. The parameter α is optimized using the gradient method. Note that a non-negative constraint is applied to the voxel value $g(\boldsymbol{r}_i)$.

The estimation of λ is important. When λ is increased, the amount of zero in the voxels is increased, or the system becomes more sparse. In this study, λ was determined using

$$\lambda = \beta \max\left(-\frac{\partial E_1^{(n)}}{\partial \boldsymbol{r}_i}\right) \tag{9}$$

with

$$E_1 = \sum_j |\eta(\boldsymbol{k}_j) - \hat{\eta}(\boldsymbol{k}_j)|^2 \tag{10}$$

and β was set to be 0.6, where the error of the fits comes to the experimental error, and λ values reach about 2.2×10^{-5} at the final conditions of the fits.

In the present calculation, the voxel size was set to be $0.01 \times 0.01 \times 0.01$ nm^3 with the distance range of ± 0.6 nm for each direction from the central Mn atom. The iteration of the L_1 regularization was started from Barton's results. The excellent improvements of the atomic images using the L_1-regularized linear regression are clearly given in Ref. [31].

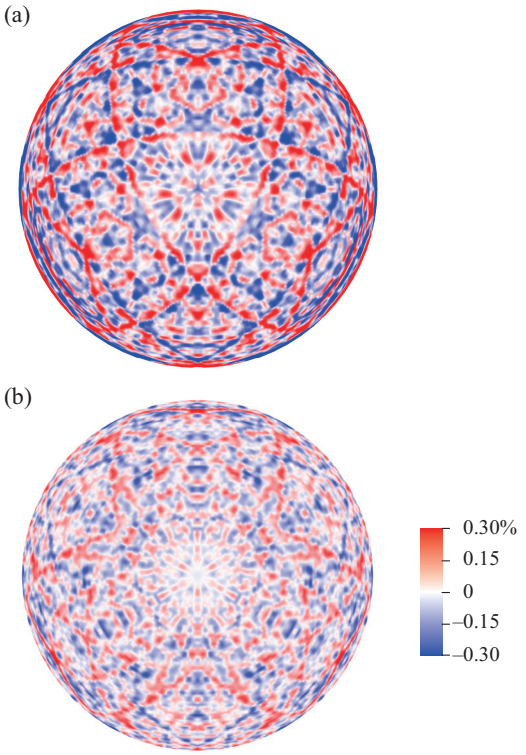

FIG. 2. Examples of the ⟨001⟩ orthogonal projection of the Mn $K\alpha$ hologram patterns of the $Bi_2Te_3Mn_{0.1}$ single crystal measured at 8.0 keV at (a) 300 K (Ref. [19]) and (b) 100 K. The radial and angle directions indicate θ and ϕ, respectively, and the magnitude is given as the color bar beside (b).

IV. RESULTS

Figure 2 shows examples of the Mn $K\alpha$ hologram patterns of the $Bi_2Te_3Mn_{0.1}$ single crystal measured at an incident x-ray energy of 8.0 keV at (a) 300 K (Ref. [19]) and (b) 100 K, which are drawn under an orthographic projection. The radial and angle directions indicate θ and ϕ, respectively, and the magnitude is given as the color bar beside (b). A roughly threefold symmetry including XSW signals was observed in the holographic patterns, indicating a good quality of the sample crystal. The amplitude of the hologram at 100 K is much weaker than that at 300 K [19]. This temperature dependence is very unusual, and complex atomic configurations are expected around the Mn impurities at 100 K.

Figure 3 shows the 3D atomic images at (a) 300 and (b) 100 K reconstructed using the SPEA-L1 algorithm. The dashed lines indicate the hexagonal structure on the (001) plane provided that the Mn impurity atom is substitutionally replaced with a Bi or Te atom in Fig. 1. At 300 K shown in Fig. 3(a), strong atomic images are observed about 0.02 nm outside the second-neighboring positions of Bi or Te atoms in the (001) plane of the central Mn atom at $z = 0$, as reported in Ref. [18] analyzed using Barton's algorithm.

In addition, many weak images appear at $z \neq 0$. However, these images do not correspond to the x-z positions of atoms, i.e., the z values of the weak images are very different from any positions suggested from the undoped Bi_2Te_3 crystal. Thus,

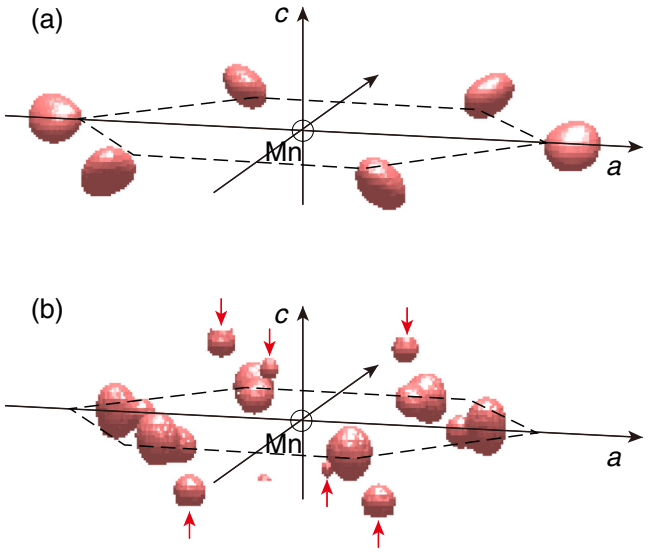

FIG. 3. 3D atomic images of the $Bi_2Te_3Mn_{0.1}$ single crystal at (a) 300 and (b) 100 K around the central Mn atom marked by the circle. Arrows indicate atomic images at $z \neq 0$.

they may be weak artifacts, and these images are removed from Fig. 3(a).

At 100 K shown in Fig. 3(b), on the other hand, the atomic images at the hexagonal positions are very weak, and instead, relatively strong images are observed inside the hexagonal positions and separated into some positions in the radial direction on the (001) plane at $z = 0$. Note that for clarity, the atomic images at 100 K are enhanced by a factor of 2 because the image intensities at 100 K are weak compared with those at 300 K, which was already expected by the weak oscillations in the hologram at 100 K shown in Fig. 2(b).

At $z \neq 0$, relatively prominent atomic images are observed at $z = \pm 0.13$ nm as shown by the arrows in Fig. 3(b). Note that these images are not hexagonal, but they have a threefold rotational symmetry that is located between the strong images at $z = 0$. It should also be noted that the direction of the triangle images at $z = 0.13$ nm is different from those at $z = -0.13$ nm.

To clarify the atomic positions and image intensities, reconstructed two-dimensional (2D) atomic images on the (001) plane are shown in Fig. 4 at (a) 300 and (b) 100 K around the central Mn atoms marked by the circles. The image intensities are normalized to that of the strongest atomic image at 300 K, and the scales are shown as the color bars beside the figures. Note that the maximum intensity at 100 K is about 70% of that at 300 K. As a guide for the eyes, intersections of dashed lines indicate ideal positions of the second-neighboring atoms obtained from x-ray diffraction (XRD) [10] provided that the central Mn atom is located at a Bi or Te position. As seen in Fig. 1, all of the atoms on the (001) plane are the same element, Bi or Te, depending on the z value along the c axis.

At 300 K shown in Fig. 4(a), prominent hexagonal atomic images are observed around the central Mn atom at a distance of 0.459 nm. The positions of the images coincide roughly with the ideal second-neighboring Bi or Te atoms of 0.4395 nm as reported in our previous paper [19]. Thus, it was concluded in

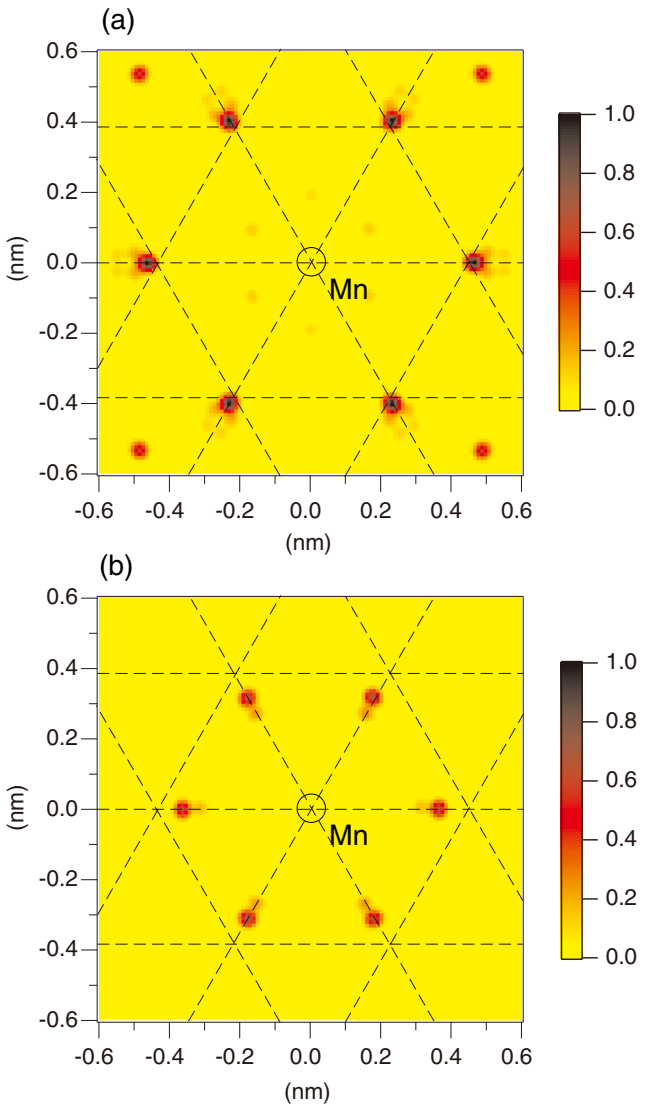

FIG. 4. 2D atomic images of the $Bi_2Te_3Mn_{0.1}$ single crystal at (a) 300 and (b) 100 K on the (001) plane around the central Mn atom marked by the circles. The intersections of dashed lines indicate ideal positions of the second neighboring atoms.

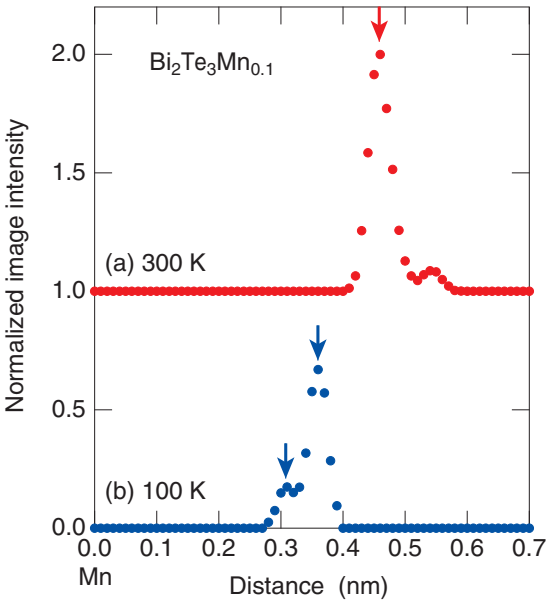

FIG. 5. The atomic image intensities along the a axis at (a) 300 and (b) 100 K. The arrows indicate the peak positions.

the last paper that the most plausible atomic position of the Mn impurities is the substitution with the Bi and/or Te atoms. From a detailed observation, however, they are located at a distance of about 0.02 nm with respect to the original Bi_2Te_3 crystal, and the image is stretched in the radial direction. Note that the atomic image obtained from an imperfect hologram is usually distorted in the angular direction [24,32,33,36]. Hence, a large positional fluctuation is expected in the radial direction.

As shown in Fig. 4(b), hexagonal atomic images are observed around the central Mn atom. Two atomic images appear inside the ideal hexagonal structure at 0.309 and 0.360 nm from the central Mn atom, along which the 0.360 nm images are strongest. Note that the intensities of these images are weaker by less than 65% than those at 300 K.

As seen in Fig. 4(b), the atomic images are slightly oval-shaped, i.e., the image sizes in the angular directions are always larger than those in the radial directions. However, it does not mean that the positional fluctuations of atoms are larger in the angular direction than those in the radial direction, but they may occur due to the lack of experimental data at $\theta = 75°$–$105°$ [24,32,33].

Figure 5 shows the normalized image intensities along the a axis at (a) 300 and (b) 100 K as a function of the distance from the central Mn atom, and the arrows indicate the peak positions. A large peak is seen at 300 K centered at 0.459 nm with the full width at half-maximum (FWHM) in the radial and angular directions of 0.021 and 0.019 (not shown) nm, respectively. On the other hand, two peaks are observed at 100 K at 0.309 and 0.360 nm with the FWHM in the radial and angular directions of about 0.018 nm and 0.020 (not shown) nm, respectively.

Figure 6 shows the atomic images of the $Bi_2Te_3Mn_{0.1}$ single crystal at 100 K on the (001) plane at (a) $z = 0.13$ and (b) -0.13 nm from the central Mn atom. Note that the colors for the intensities of these images are much weaker by about one-fifth than those at $z = 0$ nm at 300 K shown in Fig. 4(a). The intersections of dashed lines indicate the Bi or Te positions on the (001) plane in undoped Bi_2Te_3 crystal. They do not show a hexagonal form as those at $z = 0$ nm, but an inverted equilateral triangle at (a) $z = 0.13$ nm and a usual one at (b) $z = -0.13$ nm. This is clear evidence for these triangle atomic images that the Mn impurity atom is not located at the substitutional positions of Bi or Te atoms with sixfold rotational symmetry, but may be at the interstitial or interlayer one.

Figure 7 shows the $k^2\chi(k)$ spectra near the Mn K absorption edge at 30, 100, 200, and 300 K. Although the measured k range is limited and the noises are seen in the high k region of the spectra, in particular at high temperatures, it is enough to obtain reasonable structural parameters for the neighboring atoms using Hanning windows in the range of 15–115 nm^{-1} indicated by dashed curves. The magnitudes of $k^2\chi(k)$ show two maxima at about 40 and 100 nm^{-1}, indicating that the

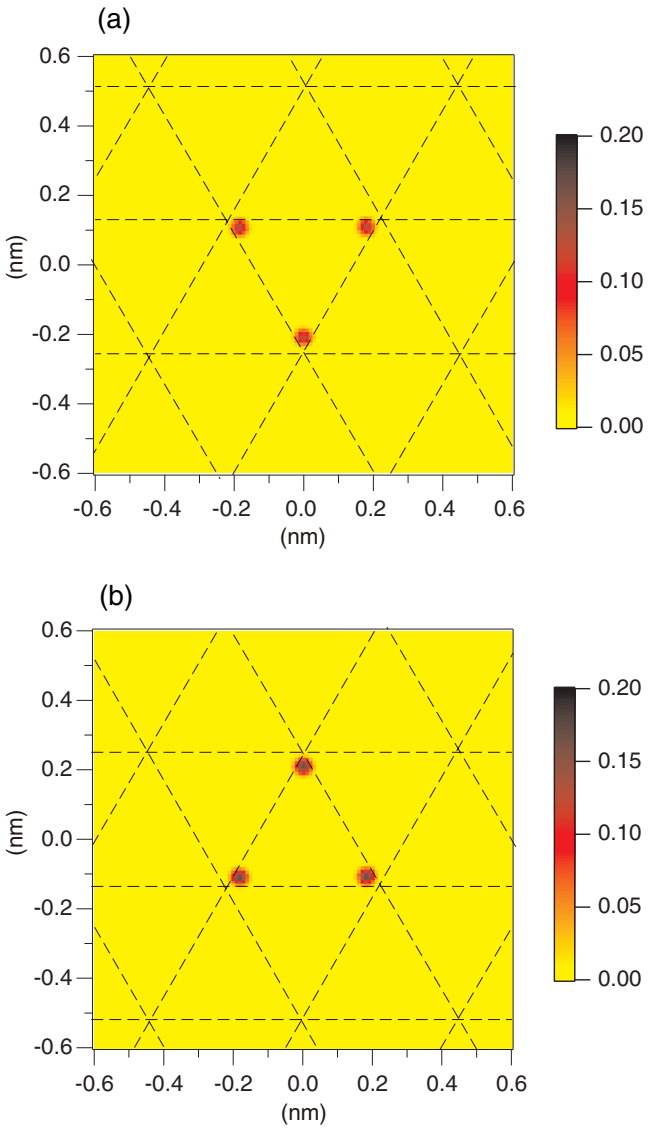

FIG. 6. Atomic images of the $Bi_2Te_3Mn_{0.1}$ single crystal at 100 K on the (001) plane at (a) $z = 0.13$ and (b) -0.13 nm. The intersections of dashed lines indicate the Te or Bi positions on the (001) plane in undoped Bi_2Te_3 crystal.

nearest-neighboring atoms are not composed of Mn but heavy elements of Bi and/or Te due to the k dependence of $f_i(k,\pi)$ for the photoelectrons.

The circles in Fig. 8 show the Fourier transforms of $k^2\chi(k)$, $|F(r)|$, experimentally obtained at 30, 100, 200, and 300 K. There are mainly three peaks in the nearest-neighboring region, i.e., at 0.225, 0.275, and 0.320 nm, where the phase shift value, $\phi_i(k)$, was not taken into account. With increasing temperature, these peak positions decrease very slightly. Note that with decreasing temperature, the small 0.225-nm peak becomes highly prominent while the other peaks gradually increase. By taking $\phi_i(k)$ of the neighboring atoms into account, the main peak at 0.275 nm seems to correspond to the nearest-neighbor Bi-Te distances of 0.3066 nm in the undoped Bi_2Te_3 crystal. Detailed assignments of these peaks are given later.

Assuming that $\phi_i(k)$ has usual values of 0.03–0.05 nm, the peaks in $|F(r)|$ seem to correspond to the peak positions in the

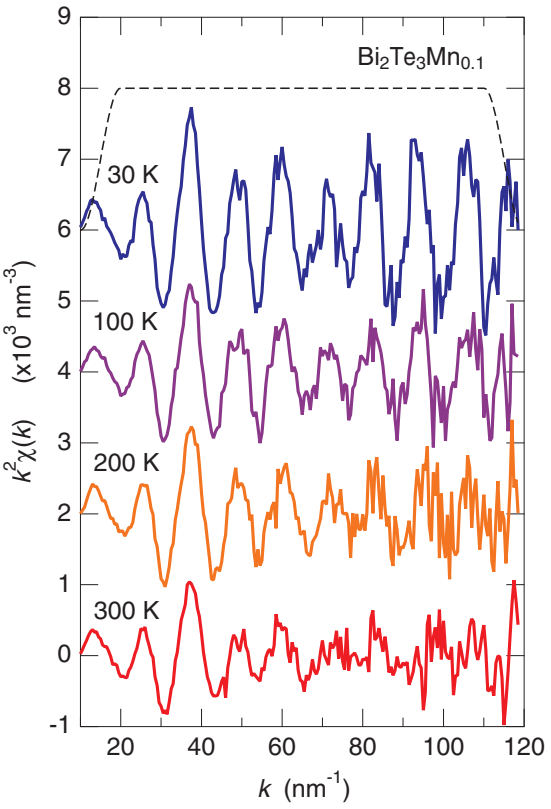

FIG. 7. The $k^2\chi(k)$ spectra near the Mn K edge XAFS measurements at 30, 100, 200, and 300 K. The dashed curve shows the Hanning window function for the Fourier transforms.

XFH data at 100 K. However, large inconsistencies are seen in the peak height, and the angular fluctuations of the neighboring atoms are highly suggested. Furthermore, the 0.5-nm peaks in the images cannot be clearly seen in $|F(r)|$, due to the limited value of the mean free path of photoelectrons and the large σ_i^2 values. Thus, further analyses for the neighboring region are necessary, and the fits to the inverse-Fourier transforms were performed using the Hanning function in the range of 0.19–0.36 nm. The results will be given in the next section.

Figure 9 shows XANES spectra around the Mn K absorption edge on the present $Bi_2Te_3Mn_{0.1}$ sample (thick curve) and several other reference samples (thin curves) of $Bi_{2-x}Mn_xTe_3$ (Refs. [9,11]), MnTe, MnO, and Mn_2O_3 (Ref. [11]). MnTe and MnO have divalent Mn cations and Mn_2O_3 trivalent ones. The XANES spectrum of the present $Bi_2Te_3Mn_{0.1}$ resembles well those of previous $Bi_{2-x}Mn_xTe_3$ alloys [9,11], and it is very similar to that of the reference MnTe with divalent Mn cation. On the other hand, the peak of the Mn_2O_3 sample with the trivalent Mn cation is shifted toward the higher energy by about 8 eV, and the overall spectral features are very different from the present result. Thus, it is concluded that the Mn atoms in Bi_2Te_3 are mostly divalent cations, as was already confirmed from core-level XPS, XAS, and XES spectra [13].

V. DISCUSSION

From the present XFH and XAFS data, a suitable model should be constructed. However, a 3D model is requested for the XAFS analysis to estimate the $f_i(k,\pi)$ and $\phi_i(k)$ functions

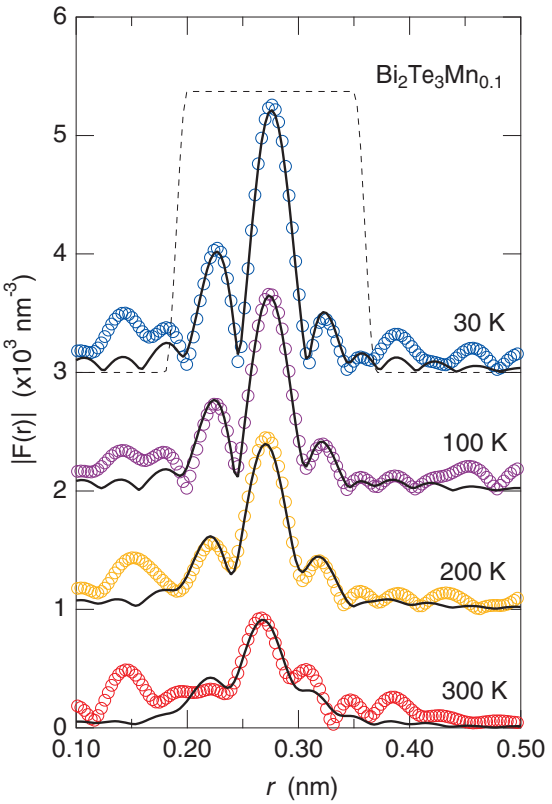

FIG. 8. The circles exhibit the $|F(R)|$ functions obtained by the XAFS measurements near the Mn K edge at 30, 100, 200, and 300 K. The dashed curve shows the Hanning window function for the inverse-Fourier transforms for further data analysis. The solid curves show the best fits using the combined model of the octahedral sites in the van der Waals gap with the substitutional site of Te(1) on the layer surface.

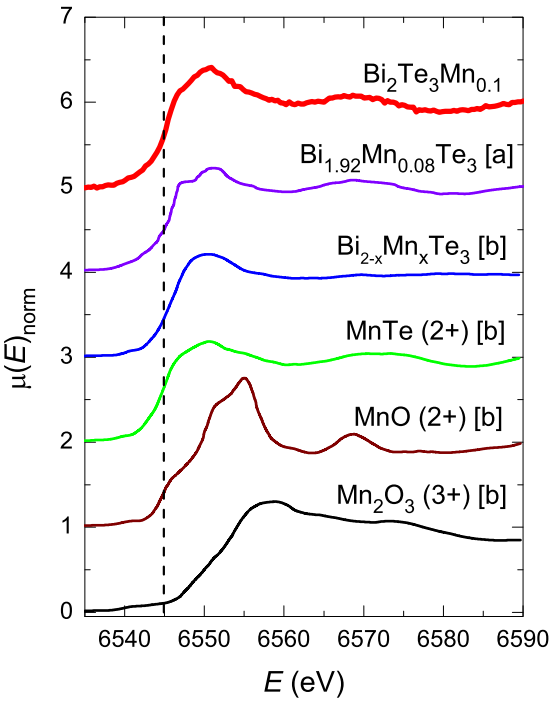

FIG. 9. XANES spectra around the Mn K edge on the present $Bi_2Te_3Mn_{0.1}$ sample (thick curve) and several other reference samples (thin curves). The reference data are taken from (a) Růžička *et al.* [9] and (b) Ghasemi *et al.* [11].

by using FEFF. Since the atomic images observed by XFH are located only on the (001) plane, the interlayer positions cannot explain the XFH data, although the interlayer positions cannot be excluded as the additional impurity sites.

We start from the 3D atomic configurations at 100 K based on the atomic images obtained by XFH shown in Figs. 3(b), 4(b), 5(b), and 6. The triangle atomic images are observed on the (001) plane at $z = \pm 0.13$ nm as shown in Fig. 6. Růžička *et al.* [9] proposed a model as shown in Fig. 10(a) that the Mn impurity atom enters an interlayer site in the van der Waals gap and forms an octahedral atomic arrangement with six Te atoms on the layer surface. In the figure, the small-, medium-, and large-sized balls indicate the Bi, Mn, and Te atoms, respectively. Since the distance between the Te atoms on the layer surfaces is 0.262 nm, and the direction of the triangles with respect to the a axis shown in Figs. 6(a) and 6(b) is correct, the impurity Mn atom may enter the interlayer octahedral site in the van der Waals gap. As shown in Fig. 6, the triangle atomic images are always located at the inner positions from the ideal Te positions indicated by the intersections of the dashed lines. Thus, small lattice shrinks are caused by the neighboring Te atoms. This result is compatible with the XRD data measured by Růžička *et al.* [9] even for the substitutional doping that by substituting 9% of the Mn atoms with Bi, the lattice parameters of the a and c axes shrink by 0.0015 nm (0.34%) and 0.0658 nm (2.18%), respectively.

The other atomic images are observed as the hexagonal shapes in the (001) plane, as shown in Figs. 3(b), 4(b), and 5(b). A plausible Mn atomic position in the Bi_2Te_3 crystal is drawn in Fig. 10 from the views of (b) parallel and (c) perpendicular directions to the c axis. The Mn atom would be substituted with a Te(1) atom in the layer surface. Since the distance from the central Mn atom is slightly shorter than that of the ideal hexagonal position, as shown above, the central Mn atom draws the Te(1) atomic position so as to make a shorter bond with the Mn-Te length with a length of mainly 0.360 nm. Due to the same hexagonal positions around the Bi and Te atoms in the undoped crystal, the above explanations are made by assuming that the impurity Mn atom is located on the Te(1) plane of the (001) plane. If the Mn site is assumed to be on the Bi or Te(2) plane, Te(1) should be replaced with Bi or Te(2) in the above model.

From the 3D atomic images obtained from the present XFH experiment, thus, one can expect that the possible Mn impurity sites are twofold, i.e., the interlayer site with the octahedral symmetry and the substitutional site of Te(1), Te(2), or Bi in the layer. Using these atomic configuration models, the consistency for the XAFS data was examined. The $f_i(k,\pi)$ and $\phi_i(k)$ functions were calculated using FEFF implanted in the Artemis program package, and the fits were performed to the inverse-Fourier-transformed $k^2\chi(k)$ functions for the neighboring atoms using a Hanning window function in the distance range $0.19 \leqslant r \leqslant 0.36$ nm with a slope of ± 0.01 nm in $|F(r)|$, as shown by the dashed curve in Fig. 8. For this analysis, the coordination numbers are fixed as obtained by

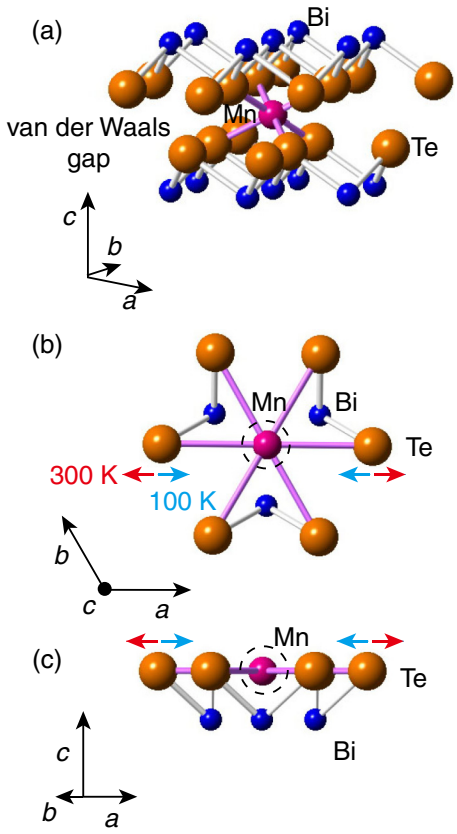

FIG. 10. Schematic views of the Mn impurity atomic positions in the undoped Bi_2Te_3 crystal. (a) The interlayer model of the octahedral pocket in the van der Waals gap, and the substitutional model with the Te(1) site viewed from the (b) parallel and (c) perpendicular directions to the c direction. The small-, medium-, and large-size balls indicate the Bi, Mn, and Te atoms, respectively, and the circles show the original Te positions replaced by the Mn impurity.

XRD. No multiple scattering contributions are included since they are likely to be negligible in the first- and second-neighboring distance range of interest.

First, we carried out the fits for the $|F(r)|$ functions using the model of only the octahedral interlayer pocket sites, and then, using the combined model of the octahedral interlayer sites with the substitutional sites of the layer surface Te [Te(1) in Fig. 1], Bi, and the middle Te [Te(2) in Fig. 1] assuming six Mn-Te(Bi) bonds as in Figs. 10(b) and 10(c). For each substitutional site model, the atoms located in the first shell region were only included for the fits of the $|F(r)|$ data, and the atoms seen as the hexagonal forms by XFH were excluded due to the very small signals in the corresponding r region of the $|F(r)|$ functions.

Table I shows the R factors obtained from the fits for the $|F(r)|$ data using the above models. As seen in the table, the substitution with the Te(1) site largely improves the fit qualities compared to without any substitutional sites except a slight deterioration at 300 K, while the fits using combined models with the Te(2) and Bi substitutional sites degrade monotonously upon increasing the fraction of the substitutional site. Note that in Table I, the R factors with

TABLE I. The R factors of the fits using the combined model of the octahedral interlayer sites with the substitutional sites of Te(1), Bi, and Te(2) in Fig. 1, and without the substitutional site with varying temperature.

T (K)	Te(1)	Te(2)	Bi	w/o
30	0.0184	0.0446	0.0503	0.0347
100	0.0151	0.0449	0.0489	0.0371
200	0.0137	0.0336	0.0511	0.0378
300	0.0713	0.0851	0.0868	0.0653

the Te(2) and Bi substitutions, as well as that with Te(1) at 300 K, have broad local minima near the fractions given later.

Thus, the most plausible model obtained from the present XFH and XAFS data is the combined model of the interlayer octahedral pocket site and the substitutional site of the Te(1) atoms in the layer surface. The solid curves in Fig. 8 indicate the best fits using the combined model. At a glance, the fit qualities are very good except at 300 K. The slight deterioration at 300 K may be due to an imperfect model for the atomic configurations around the Mn impurity atom at 300 K, and it may be related to the change of the atomic images on the (001) plane shown in Figs. 4(a) and 4(b). For the substitutional Te(1) site in the combined model, the Mn-Bi interatomic distance in the layer, r_{MnBi}, is obtained as 0.3153 nm (averaged over the measured temperatures), slightly longer than the $r_{\mathrm{Te(1)\text{-}Bi}}$ value of 0.3065 nm in the undoped crystal [10]. On the other hand, the $r_{\mathrm{MnTe(1)}}$ one with the neighboring layer is 0.3588 nm, slightly shorter than the $r_{\mathrm{Te(1)Te(1)}}$ value of 0.3647 nm [10], which also supports the shrinkage of the lattice parameters by doping.

Figure 11(a) exhibits the fraction of the octahedral interlayer sites as a function of temperature, which was calculated using the combined model for the XAFS data. The fraction of the octahedral sites reaches about 60%, and the remaining 40% corresponds to the Te(1) substitutional sites at all the temperatures, and seems to be mostly unchanged with temperature.

Figure 11(b) shows the bond lengths, r_{ij}, of Mn-Bi (empty triangles) and Mn-Te (empty inverted triangles) in the octahedral interlayer sites as a function of temperature, which were calculated using the combined model for the XAFS data. The left arrows indicate the r_{ij} values of 0.304 and 0.292 nm obtained by Růžička *et al.* [9] using only the octahedral model for the Mn-Bi and Mn-Te interatomic distances, respectively, at room temperature, which are slightly longer than the present results with the combined model. With increasing temperature, r_{MnBi} in the octahedral interlayer sites increases, while r_{MnTe} decreases. A complex atomic rearrangement may be necessary to explain these temperature dependences.

Figure 11(c) shows the square of the Debye-Waller factors, σ_{ij}^2, of Mn-Bi (empty triangles) and Mn-Te (empty inverted triangles) in the octahedral interlayer site, and Mn-Bi in the substitutional layer surface (solid symbols) sites, as a function of temperature, which were calculated using the combined model for the XAFS data. The Mn-Bi and Mn-Te bonds in the octahedral interlayer sites show mostly the same small σ_{ij}^2 values, while the Mn-Te bond in the substitutional surface

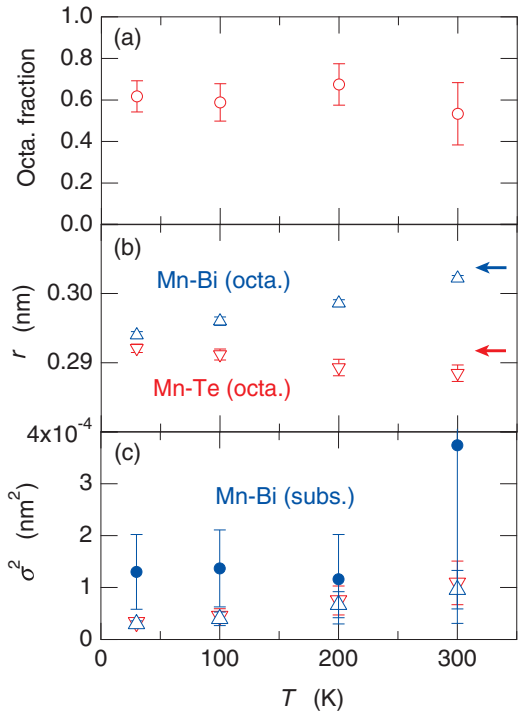

FIG. 11. Temperature dependence of (a) the fraction of the octahedral interlayer sites, (b) r_{ij} around the octahedral interlayer site, and (c) σ_{ij}^2 of the octahedral (empty symbols) and Te(1) substitutional layer surface (solid symbols) sites.

site exhibits much larger σ_{ij}^2 values. This is due, again, to the difference of the bonding natures of a rigid octahedron and a flexible layer surface. All of the σ_{ij}^2 values increase with increasing temperature, as usual.

At 100 K, the information about the positions of impurity Mn atoms are clearly obtained from the present XFH and XAFS experiment using the present combination model. We found two possible sites for the Mn impurities, i.e., an interlayer site with an octahedral symmetry and a substitutional site of Te(1) on the layer surface, and the fraction is about 3:2. This is experimental proof that there are two impurity sites in TM-doped Bi_2X_3. From the viewpoint of the TI nature, the substitution of Te(1) causes the additional Te atoms in Bi_2Te_3, i.e., $Bi_2Te_{3+\delta}$, which produces the electronic change from a p-type degenerate semiconductor to a TI.

At 300 K, however, the impurity positions were not clarified well. Namely, atomic images by XFH are located only in strong hexagonal ring form, and the errors of the best fits for the $|F(r)|$ function by XAFS are much larger by about four times than those at low temperatures. Moreover, there is no overlap in the r region for the knowledge obtained from XFH and XAFS, i.e., the information from XFH is beyond 0.4 nm, while that from XAFS is limited until about 0.35 nm. Thus, our knowledge on the Mn positions at 300 K could not be enriched by adding the XAFS data.

Furthermore, the reasons for the anomalous temperature dependence and shift of the atomic positions in the hexagonal second-neighboring Te(1) lattice are still unclear. Based on the present XFH images combined with the XAFS data, we speculate a possible structure around the Mn atoms. The expanded Te(1) hexagonal ring may be unchanged with temperature, although it is not unclear why Te(1) atoms like to form the larger ring around the Mn impurity. At 300 K, the Mn impurity is located at the center of the ring. Thus, clear hexagonal atomic images are observed as in Fig. 4(a). Small positional fluctuations of the central Mn atom are observed as the oval shape of the Te(1) images in the radial direction.

At 100 K, on the other hand, the large shifts of the central Mn atom may occur by 0.1 nm toward one of the Te(1) atoms. Thus, the image intensities of the Te(1) atoms are highly reduced, unlike the usual temperature dependence. If this speculation is correct and the atomic positions of the hexagonal ring are rigid, six weak atomic images may appear around each of the hexagonal atomic images at 300 K. Due to self-organizations of the Te(1) atomic positions, however, only one image can be selectively observed in the XFH image shown in Fig. 4(b).

Our present combined model for the impurity sites is in good agreement with the existing models by Růžička *et al.* [9] and Ghasemi *et al.* [11], concerning the impurity sites in the van der Waals gap between the layers. In addition, the latter article shows the experimental proof that the Mn substitution of Te occurs with the increased Mn concentration of more than 6%, mostly corresponding to the concentration of the present XFH and XAFS measurements, although the doping manners of substitutional and additional are different.

To explain how it is energetically possible that the Mn impurity atoms enter the interstitial and substitutional sites in Bi_2Te_3, Ghasemi *et al.* [11] carried out *ab initio* MD simulations with 16 different atomic configurations. For the interstitial site in the van der Waals gap, the octahedral sites are energetically much more favorable than the tetrahedral sites, which is another pocket in the van der Waals gap. For the Bi substitution, the most favorable configuration is when the Mn atoms occupy the closest Bi sites in two different Bi layers. For the Te substitution, the Mn atoms are most stable when occupying the furthest Te(1) and Te(2) sites.

It should, however, be noted that our sample is a bulk-grown crystal manufactured at a high temperature, whereas their samples are epitaxial films grown using MBE at a lower temperature. Thus, it is possible that the impurity sites are different from each other due to the thermal history. Since XFH enables us to measure 3D atomic images of thin films without any additional techniques [24,34,35], we will be able to obtain the same quality of the local structure and examine the differences between the bulk and thin-film samples.

For further investigations on the Mn impurity positions in the Te(1) substitutional site, an XFH experiment at much lower temperatures may be essential, since the atomic positions are quite stabilized and the XFH images are expected to be much stronger and sharper. For this, we are preparing an XFH setup in which the ϕ rotational equipment should be located in a cryostat.

It should be noted that the first problem on the nearest-neighboring image listed in the Introduction still remains unsolved. The nearest-neighboring Bi atoms can be detected in the XAFS data, and the radial positional fluctuations are not so usual, as shown in Fig. 11(c). Moreover, large positional fluctuations are expected in the angular direction. It can be speculated that the reason why the Bi images are invisible in

the XFH results is the positional fluctuations with respect to the central Mn atom. The large decrease of the atomic images by the angular atomic fluctuations was pointed out for the Ga-doped InSb crystal around the impurity Ga atoms [36].

Finally, we would like to emphasize that these findings for the impurity sites cannot be obtained by diffraction or XAFS experiment in the usual way, due, respectively, to the lack of long-range periodicity or that of three-dimensional information. Only using a combination of the XFH and XAFS measurements, such a long-standing problem can be solved without any ambiguity, at least at 100 K.

VI. CONCLUSION

Mn $K\alpha$ XFH measurements were performed on a $Bi_2Te_3Mn_{0.1}$ TI single crystal at 100 and 300 K to search for the sites of the Mn impurities in this functional crystal. XAFS experiments at 30–300 K are also used for further investigations. We found two possible sites for the Mn impurities, i.e., an interlayer site with octahedral symmetry and a substitutional site of Te(1) on the layer surface. For this finding, the data analysis using the L_1-regularized linear regression was very effective to reduce the artifacts in the XFH images. Local structural information was obtained by detailed analyses for the present XFH and XAFS data, such as the ratio of the Mn impurity sites, the Mn-Te interatomic distances, the lattice distortions, and the positional fluctuations around the impurity Mn atoms. Distinct temperature dependences are seen in both the XFH and XAFS data, and the positional fluctuations are expected around the impurity Mn atoms.

ACKNOWLEDGMENTS

The authors thank Ichiro Akai and Masato Okada for the useful information on the sparse modeling. The present XFH experiments were performed at BL6C of PF-KEK (No. 2013G605) and the supporting experiments were carried out at BL09XU (No. 2013B1275 and No. 2014A1065) and BL12B2 (No. 2013B4125, No. 2014B4125, and No. 2015A4134) of SPring-8. The XAFS experiments were performed at BL11 of Kyushu Synchrotron Light Research Center (No. 1403005F and No. 1503016F). This work was supported by JSPS Grant-in-Aid for Scientific Research (B) (No. 17H02814), and those on Innovative Areas "3D Active-Site Science" (No. 26105006 and No. 26105013) and "Sparse modeling" (No. 16H01553). J.R.S. gratefully acknowledges financial support as Overseas Researcher under a JSPS fellowship (No. P16796).

[1] R. Venkatasubramanian, E. Siivola, T. Colpitts, and B. O'Quinn, Nature (London) **413**, 597 (6856).
[2] G. J. Snyder and E. S. Toberer, Nat. Mater. **7**, 105 (2008).
[3] H.-J. Kim, K.-S. Kim, M. D. Kim, S.-J. Lee, J.-W. Han, A. Ohnishi, M. Kitaura, M. Sasaki, A. Kondo, and K. Kindo, Phys. Rev. B **84**, 125144 (2011).
[4] H. Zhang, C.-X. Liu, X.-L. Qi, X. Dai, Z. Fang, and S.-C. Zhang, Nat. Phys. **5**, 438 (2009).
[5] V. A. Greanya, W. C. Tonjes, R. Liu, C. G. Olson, D.-Y. Chung, and M. G. Kanatzidis, Phys. Rev. B **62**, 16425 (2000).
[6] Y. L. Chen, J. G. Analytis, J.-H. Chu, Z. K. Liu, S.-K. Mo, X. L. Qi, H. J. Zhang, D. H. Lu, X. Dai, Z. Fang, S. C. Zhang, I. R. Fisher, Z. Hussain, and Z.-X. Shen, Science **325**, 178 (2009).
[7] H.-J. Noh, H. Koh, S.-J. Oh, J.-H. Park, H.-D. Kim, J. D. Rameau, T. Valla, T. E. Kidd, P. D. Johnson, Y. Hu, and Q. Li, Europhys. Lett. **81**, 57006 (2008).
[8] H.-J. Kim, K.-S. Kim, J.-F. Wang, V. A. Kulbachinskii, K. Ogawa, M. Sasaki, A. Ohnishi, M. Kitaura, Y.-Y. Wu, L. Li, I. Yamamoto, J. Azuma, M. Kamada, and V. Dobrosavljević, Phys. Rev. Lett. **110**, 136601 (2013).
[9] J. Růžička, O. Caha, V. Holý, H. Steiner, V. Volobuiev, A. Ney, G. Bauer, T. Duchoň, K. Veltruská, I. Khalakhan, V. Matolín, E. F. Schwier, H. Iwasawa, K. Shimada, and G. Springholz, New J. Phys. **17**, 013028 (2015).
[10] Y. Feutelais, B. Legendre, N. Rodier, and V. Agafonov, Mater. Res. Bull. **28**, 591 (1993).
[11] A. Ghasemi, D. Kepaptsoglou, A. I. Figueroa, G. A. Naydenov, P. J. Hasnip, M. I. J. Probert, Q. Ramasse, G. van der Laan, T. Hesjedal, and V. K. Lazarov, APL Mater. **4**, 126103 (2016).
[12] K. Carva, J. Kudrnovský, F. Máca, V. Drchal, I. Turek, P. Baláž, V. Tkáč, V. Holý, V. Sechovský, and J. Honolka, Phys. Rev. B **93**, 214409 (2016).
[13] B. Leedahl, D. W. Boukhvalov, E. Z. Kurmaev, A. Kukharenko, I. S. Zhidkov, N. V. Gavrilov, S. O. Cholakh, P. H. Le, C. W. Luo, and A. Moewes, Sci. Rep. **7**, 5758 (2017).
[14] Z. Liu, X. Wei, J. Wang, H. Pan, F. Ji, F. Xi, J. Zhang, T. Hu, S. Zhang, Z. Jiang, W. Wen, Y. Huang, M. Ye, Z. Yang, and S. Qiao, Phys. Rev. B **90**, 094107 (2014).
[15] A. Polyakov, H. L. Meyerheim, E. D. Crozier, R. A. Gordon, K. Mohseni, S. Roy, A. Ernst, M. G. Vergniory, X. Zubizarreta, M. M. Otrokov, E. V. Chulkov, and J. Kirschner, Phys. Rev. B **92**, 045423 (2015).
[16] A. I. Figueroa, G. van der Laan, L. J. Collins-McIntyre, S.-L. Zhang, A. A. Baker, S. E. Harrison, P. Schönherr, G. Cibin, and T. Hesjedal, Phys. Rev. B **90**, 134402 (2014).
[17] A. I. Figueroa, G. van der Laan, L. J. Collins-McIntyre, G. Cibin, A. J. Dent, and T. Hesjedal, J. Phys. Chem. C **119**, 17344 (2015).
[18] K. Hayashi, N. Happo, S. Hosokawa, W. Hu, and T. Matsushita, J. Phys.: Condens. Matter **24**, 093201 (2012).
[19] S. Hosokawa, N. Happo, K. Hayashi, A. Ohnishi, M. Kitaura, and M. Sasaki, J. Phys.: Conf. Ser. **502**, 012024 (2014).
[20] G. I. Makovetskii, A. I. Galyas, G. M. Severin, and K. I. Yanushkevich, Inorg. Mater. **32**, 846 (1996).
[21] E. Janik, E. Dynowska, J. Bąk-Misiuk, M. Leszczyński, W. Szuszkiewicz, T. Wojtowicz, G. Karczewski, A. K. Zakrzewski, and J. Kossut, Thin Solid Films **267**, 74 (1995).
[22] M. Mimasaka, I. Sakamoto, K. Murata, Y. Fujii, and A. Onodera, J. Phys. C **20**, 4689 (1987).
[23] J. J. Barton, Phys. Rev. Lett. **67**, 3106 (1991).
[24] S. Hosokawa, N. Happo, S. Senba, T. Ozaki, T. Matsushita, A. Koura, F. Shimojo, and K. Hayashi, J. Phys. Soc. Jpn. **83**, 124602 (2014).
[25] N. Happo, K. Hayashi, and S. Hosokawa, Jpn. J. Appl. Phys. **49**, 116601 (2010).

[26] T. Matsushita, e-J. Surf. Sci. Nanotech. **14**, 158 (2016).
[27] B. Ravel and M. Newville, J. Synch. Radiat. **12**, 537 (2005).
[28] S. I. Zabinsky, J. J. Rehr, A. Ankudinov, R. C. Albers, and M. J. Eller, Phys. Rev. B **52**, 2995 (1995).
[29] C. M. Bishop, *Pattern Recognition and Machine Learning* (Springer, New York, 2007).
[30] T. Matsushita, F. Z. Guo, M. Suzuki, F. Matsui, H. Daimon, and K. Hayashi, Phys. Rev. B **78**, 144111 (2008).
[31] T. Matsushita, T. Muro, F. Matsui, N. Happo, S. Hosokawa, K. Ohoyama, A. Sato-Tomita, Y. C. Sasaki, and K. Hayashi (unpublished).
[32] T. Matsushita, A. Agui, and A. Yoshigoe, Europhys. Lett. **65**, 207 (2004).
[33] T. Matsushita, F. Matsui, H. Daimon, and K. Hayashi, J. Electron Spectrosc. Relat. Phenom. **178-179**, 195 (2010).
[34] K. Hayashi, N. Uchitomi, K. Yamagami, A. Suzuki, H. Yoshizawa, J. T. Asubar, N. Happo, and S. Hosokawa, J. Appl. Phys. **119**, 125703 (2016).
[35] N. Happo, K. Hayashi, S. Senba, H. Sato, M. Suzuki, and S. Hosokawa, J. Phys. Soc. Jpn. **83**, 113601 (2014).
[36] S. Hosokawa, N. Happo, T. Ozaki, H. Ikemoto, T. Shishido, and K. Hayashi, Phys. Rev. B **87**, 094104 (2013).